Research Article | Vol. 26, No. 6 | 19 Mar 2018 | OPTICS EXPRESS 7563
Optics EXPRESS

Computational localization microscopy with extended axial range

YONGZHUANG ZHOU, PAUL ZAMMIT, GUILLEM CARLES, AND ANDREW R. HARVEY*

School of Physics & Astronomy, University of Glasgow, Glasgow G12 8QQ, UK
**andy.harvey@glasgow.ac.uk*

Abstract: A new single-aperture 3D particle-localization and tracking technique is presented that demonstrates an increase in depth range by more than an order of magnitude without compromising optical resolution and throughput. We exploit the extended depth range and depth-dependent translation of an Airy-beam PSF for 3D localization over an extended volume in a single snapshot. The technique is applicable to all bright-field and fluorescence modalities for particle localization and tracking, ranging from super-resolution microscopy through to the tracking of fluorescent beads and endogenous particles within cells. We demonstrate and validate its application to real-time 3D velocity imaging of fluid flow in capillaries using fluorescent tracer beads. An axial localization precision of 50 nm was obtained over a depth range of 120μm using a 0.4NA, 20× microscope objective. We believe this to be the highest ratio of axial range-to-precision reported to date.

OCIS codes: (180.6900) Three-dimensional microscopy; (100.4999) Pattern recognition, target tracking; (110.1758) Computational imaging; (110.7348) Wavefront encoding; (180.2520) Fluorescence microscopy.

References and links

1. M. J. Rust, M. Bates, and X. Zhuang, "Sub-diffraction-limit imaging by stochastic optical reconstruction microscopy (STORM)," Nat. Methods **3**(10), 793–796 (2006).
2. E. Betzig, G. H. Patterson, R. Sougrat, O. W. Lindwasser, S. Olenych, J. S. Bonifacino, M. W. Davidson, J. Lippincott-Schwartz, and H. F. Hess, "Imaging intracellular fluorescent proteins at nanometer resolution," Science **313**(5793), 1642–1645 (2006).
3. V. Levi and E. Gratton, "Exploring dynamics in living cells by tracking single particles," Cell Biochem. Biophys. **48**(1), 1–15 (2007).
4. C. Bustamante, S. B. Smith, J. Liphardt, and D. Smith, "Single-molecule studies of DNA mechanics," Curr. Opin. Struc. Biol. **10**(3), 279–285 (2000).
5. C. E. Towers, D. P. Towers, H. I. Campbell, S. Zhang, and A. H. Greenaway, "Three-dimensional particle imaging by wavefront sensing," Opt. Lett. **31**(9), 1220–1222 (2006).
6. L. Holtzer, T. Meckel, and T. Schmidt, "Nanometric three-dimensional tracking of individual quantum dots in cells," Appl. Phys. Lett. **90**(5), 053902 (2007).
7. E. Toprak, H. Balci, B. H. Blehm, and P. R. Selvin, "Three-dimensional particle tracking via bifocal imaging," Nano Lett. **7**(7), 2043–2045 (2007).
8. M. F. Juette, T. J. Gould, M. D. Lessard, M. J. Mlodzianoski, B. S. Nagpure, B. T. Bennett, S. T. Hess, and J. Bewersdorf, "Three-dimensional sub-100 nm resolution fluorescence microscopy of thick samples," Nat. Methods **5**(6), 527–529 (2008).
9. Y. Shechtman, S. J. Sahl, A. S. Backer, and W. E. Moerner, "Optimal point spread function design for 3D imaging," Phys. Rev. Lett. **113**(13), 133902 (2014).
10. Y. Shechtman, L. E. Weiss, A. S. Backer, S. J. Sahl, and W. E. Moerner, "Precise three-dimensional scan-free multiple-particle tracking over large axial ranges with tetrapod point spread functions," Nano Lett. **15**(6), 4194–4199 (2015).
11. F. Huang, G. Sirinakis, E. S. Allgeyer, L. K. Schroeder, W. C. Duim, E. B. Kromann, T. Phan, F. E. Rivera-Molina, J. R. Myers, I. Irnov, M. Lessard, Y. Zhang, M. Handel, C. Jacobs-Wagner, C. P. Lusk, J. E. Rothman, D. Toomre, M. J. Booth, and J. Bewersdorf, "Ultra-high resolution 3D imaging of whole cells," Cell **166**(4), 1028–1040 (2016).
12. B. Huang, W. Wang, M. Bates, and X. Zhuang, "Three-dimensional super-resolution imaging by stochastic optical reconstruction microscopy," Science **319**(5864), 810–813 (2008).

#314724 https://doi.org/10.1364/OE.26.007563
Journal © 2018 Received 30 Nov 2017; revised 14 Feb 2018; accepted 15 Feb 2018; published 15 Mar 2018

Optics EXPRESS

13. R. Piestun, Y. Y. Schechner, and J. Shamir, "Propagation-invariant wave fields with finite energy," J. Opt. Soc. Am. A **17**(2), 294–303 (2000).
14. F. Pereira, M. Gharib, D. Dabiri, and D. Modarress, "Defocusing digital particle image velocimetry: a 3-component 3-dimensional DPIV measurement technique. application to bubbly flows," Exp. Fluids **29**(1), S078–S084 (2000).
15. S. Chen, N. Angarita-Jaimes, D. Angarita-Jaimes, B. Pelc, A. H. Greenaway, C. E. Towers, D. Lin, and D. P. Towers, "Wavefront sensing for three-component three-dimensional flow velocimetry in microfluidics," Exp. Fluids **47**(4), 849–863 (2009).
16. M. V. Berry and N. L. Balazs, "Nonspreading wave packets," Am. J. Phys. **47**(3), 264–267 (1979).
17. G. A. Siviloglou, J. Broky, A. Dogariu, and D. N. Christodoulides, "Observation of accelerating airy beams," Phys. Rev. Lett. **99**(21), 213901 (2007).
18. P. Zammit, A. R. Harvey, and G. Carles, "Extended depth-of-field imaging and ranging in a snapshot," Optica **1**(4), 209–216 (2014).
19. P. Zammit, "Extended depth-of-field imaging and ranging in microscopy," Ph.D. thesis, University of Glasgow (2016).
20. H. P. Kao and A. S. Verkman, "Tracking of single fluorescent particles in three dimensions: use of cylindrical optics to encode particle position," Biophys. J. **67**(3), 1291–1300 (1994).
21. C. Cierpka and C. J. Kähler, "Particle imaging techniques for volumetric three-component (3D3C) velocity measurements in microfluidics," J. Visual. **15**(1), 1–31 (2012).
22. C. E. Willert and M. Gharib, "Three-dimensional particle imaging with a single camera," Exp. Fluids **12**(6), 353–358 (1992).
23. F. Pereira and M. Gharib, "Defocusing digital particle image velocimetry and the three-dimensional characterization of two-phase flows," Meas. Sci. Technol. **13**(5), 683–694 (2002).
24. S. Y. Yoon and K. C. Kim, "3D particle position and 3D velocity field measurement in a microvolume via the defocusing concept," Meas. Sci. Technol. **17**(11), 2897–2905 (2006).
25. S. R. P. Pavani and R. Piestun, "High-efficiency rotating point spread functions," Opt. Express **16**(5), 3484–3489 (2008).
26. H. D. Lee, S. J. Sahl, M. D. Lew, and W. E. Moerner, "The double-helix microscope super-resolves extended biological structures by localizing single blinking molecules in three dimensions with nanoscale precision," Appl. Phys. Lett. **100**(15), 153701 (2012).
27. S. R. P. Pavani, M. A. Thompson, J. S. Biteen, S. J. Lord, N. Liu, R. J. Twieg, R. Piestun, and W. E. Moerner, "Three-dimensional, single-molecule fluorescence imaging beyond the diffraction limit by using a double-helix point spread function," Proc. Natl. Acad. Sci. U.S.A. **106**(9), 2995–2999 (2009).
28. G. Grover, S. Quirin, C. Fiedler, and R. Piestun, "Photon efficient double-helix PSF microscopy with application to 3D photo-activation localization imaging," Biomed. Opt. Express **2**(11), 3010–3020 (2011).
29. M. A. Thompson, M. D. Lew, and W. E. Moerner, "Extending microscopic resolution with single-molecule imaging and active control," Ann. Rev. Biophys. **41**(1), 321–342 (2012).
30. W. E. Moerner, "Microscopy beyond the diffraction limit using actively controlled single molecules," J. Microsc. **246**(3), 213–220 (2012).
31. C. P. Calderon, M. A. Thompson, J. M. Casolari, R. C. Paffenroth, and W. E. Moerner, "Quantifying transient 3D dynamical phenomena of single mRNA particles in live yeast cell measurements," J. Phys. Chem. B **117**(49), 15701–15713 (2013).
32. B. Yu, J. Yu, W. Li, B. Cao, H. Li, D. Chen, and H. Niu, "Nanoscale three-dimensional single particle tracking by light-sheet-based double-helix point spread function microscopy," Appl. Opt. **55**(3), 449–453 (2016).
33. J. Yajima, K. Mizutani, and T. Nishizaka, "A torque component present in mitotic kinesin Eg5 revealed by three-dimensional tracking," Nat. Struct. Mol. Biol. **15**(10), 1119–1121 (2008).
34. Y. Sun, J. D. McKenna, J. M. Murray, E. M. Ostap, and Y. E. Goldman, "Parallax: High accuracy three-dimensional single molecule tracking using split images," Nano Lett. **9**(7), 2676–2682 (2009).
35. A. S. Backer, M. P. Backlund, A. R. Von Diezmann, S. J. Sahl, and W. E. Moerner, "A bisected pupil for studying single-molecule orientational dynamics and its application to three-dimensional super-resolution microscopy," Appl. Phys. Lett. **104**(19), 161103 (2014).
36. S. Jia, J. C. Vaughan, and X. Zhuang, "Isotropic three-dimensional super-resolution imaging with a self-bending point spread function," Nat. Photonics **8**, 302–306 (2014).
37. T. Vettenburg, N. Bustin, and A. R. Harvey, "Fidelity optimization for aberration-tolerant hybrid imaging systems," Opt. Express **18**(9), 9220–9228 (2010).
38. E. R. Dowski and W. T. Cathey, "Extended depth of field through wave-front coding," Appl. Opt. **34**(11), 1859–1866 (1995).
39. G. Muyo and A. R. Harvey, "Decomposition of the optical transfer function: wavefront coding imaging systems," Opt. Lett. **30**(20), 2715–2717 (2005).
40. K. Adelsberger, "Design guidelines for wavefront coding in broadband optical systems," Ph.D. thesis, University of Rochester (2014).
41. Y. Wu, L. Dong, Y. Zhao, M. Liu, X. Chu, W. Jia, X. Guo, and Y. Feng, "Analysis of wavefront coding imaging with cubic phase mask decenter and tilt," Appl. Opt. **55**(25), 7009–7017 (2016).
42. B. Shuang, J. Chen, L. Kisley, and C. F. Landes, "Troika of single particle tracking programing: SNR enhancement,

Optics EXPRESS

particle identification, and mapping," Phys. Chem. Chem. Phys. **16**(2), 624–634 (2014).
43. K. Jaqaman, D. Loerke, M. Mettlen, H. Kuwata, S. Grinstein, S. L. Schmid, and G. Danuser, "Robust single-particle tracking in live-cell time-lapse sequences," Nat. methods **5**(8), 695–702 (2008).
44. "Depth of field and depth of focus," Available at https://www.microscopyu.com/microscopy-basics/depth-of-field-and-depth-of-focus. Accessed: 2016-12-16.
45. D. Lin, N. C. Angarita-Jaimes, S. Chen, A. H. Greenaway, C. E. Towers, and D. P. Towers, "Three-dimensional particle imaging by defocusing method with an annular aperture," Opt. Lett. **33**(9), 905–907 (2008).
46. J. C. Crocker and D. G. Grier, "Methods of digital video microscopy for colloidal studies," J. Colloid Interf. Sci. **179**(1), 298–310 (1996).
47. J. Štigler, "Analytical velocity profile in tube for laminar and turbulent flow," Engineer. Mechan. **21**(6), 371–379 (2014).
48. J. Lu, F. Pereira, S. E. Fraser, and M. Gharib, "Three-dimensional real-time imaging of cardiac cell motions in living embryos," J. Biomed. Opt. **13**(1), 014006 (2008).

1. Introduction

Diffraction is perhaps the major factor limiting high-resolution microscopy of biological samples. For a large numerical aperture (NA), diffraction limits transverse spatial resolution to about half a wavelength of light (that is about 200 nm) and to an in-focus plane that is less than a micron thick. Point sources can however be localized with a precision that can be much better than the diffraction limit (as small as a few nm) and this is the basis of recent rapid progress in localization microscopy techniques such as stochastic optical reconstruction microscopy (STORM) [1] and photo-activated localization microscopy (PALM) [2]. Similarly, localization and tracking of single fluorescent endogenous particles within cells [3] or of fluorescent beads [4] has enabled fundamental studies on cell dynamics and processes, as well as applications including micro-particle tracking velocimetry (μ-PTV) for microfluidic dynamics characterizations, lab-on-chip experiments and *in vivo* imaging [5–7]. Precise localization using conventional microscopy is nevertheless limited by diffraction to thin planes of about a micron thick, which prevents localization of points in three dimensions over extended depth ranges. The need to understand complex biological structures has stimulated research into localization of particles in three-dimensions in thick samples [8–11]; typically by exploiting characteristic axial variations in the optical point-spread function (PSF) [6, 7, 12–14]. Previously reported techniques suffer from a fundamental limit of microscopy: high transverse resolution requires a high NA for the objective, which necessarily results in a small depth-of-field (DOF), and hence a small depth range over which adequately precise localization is possible. For a typical system employing a 20× objective lens to yield localization precision of better than 100 nm, the axial range is limited to less than 10 μm [15], which is comparable to cell dimensions and is smaller than many biological structures of interest.

We propose here a technique that exploits the accelerating translation of Airy beams [16, 17] and image recovery based on complementary-kernel matching (CKM) [18, 19], which offers the ability to localize particles with a precision comparable to that of conventional techniques, but with an order-of-magnitude increase in depth range. We report the demonstration of an extended-range particle-tracking velocimetry in microfluidic systems, but the technique may be easily applied to a wide range of particle-localization applications, including *in vivo* and *in vitro* imaging and 3D super-resolution microscopy as described above.

One of the earliest single-aperture configurations for 3D particle tracking, introduced by Kao et al. in 1994 [20], employed an astigmatic PSF. The transverse dimension and ellipticity of the PSF enable determination of the magnitude and sign of axial displacement of particles from nominal focus. This technique has found broad employment, such as in the tracking of individual quantum dots in cells [6], μ-PTV in micro-channel chips [15] and super-resolution microscopy [12]. Significant disadvantages, however, are that the rapid increase in size of the PSF with defocus reduces the signal-to-noise ratio (SNR), limiting the depth range and the seeding concentration [21]. Particle localization can also be achieved by triangulation of the three lobes formed when a three-pinhole mask is located close to the pupil [14, 22–24]. The orientation and

Optics EXPRESS

scale of the resultant triplet PSF yields the sign and magnitude of the defocus parameter, which is more robust than measuring the eccentricity of an elliptical PSF. This configuration was first realized in measurements of fluid flow in a vortex ring [22] and then adopted for application in microfluidics [24]. The use of the pinhole mask in the pupil severely limits the NA of the system however, which in turn lowers both the optical throughput, the SNR [21] and precision. The particle concentration is also compromised by the expansion of the triplet PSF at large defocus.

An alternative way of performing 3D particle localization with a single aperture is the engineered PSF. One such approach is the Double-helix PSF (DH-PSF), which is generated by superimposing a specific subset of Gauss-Laguerre modes [13]. This results in a PSF where most of the energy is concentrated in two main lobes which rotate about a common center with changing defocus [25]. The depth information is then encoded in the orientation of the lobes. The DH-PSF has been widely used in super-resolution microscopy and single-molecule localization experiments [26–30], and has recently been employed for 3D particle tracking in both live cells and microfluidic devices [31, 32]. The DH-PSF is operable over an extended depth range compared to the previously-discussed techniques, but due to its symmetry, the maximum unambiguous rotation angle is limited to 180°requiring a limitation in the depth range and implying that the DH-PSF suffers from a trade-off between the range and the responsivity ($\partial z/\partial\theta$) and therefore, of the axial precision.

Image translations associated with the beams produced by specialized pupil phase functions or using parallax can also be exploited for 3D localization [33–36]. A remarkable example was reported by Jia et al. on the use of a custom, self-bending PSF (SB-PSF) generated by introduction of a truncated cubic phase function using a spatial-light modulator (SLM) and polarization manipulation to form two replicated images of point sources on a single detector [36]. The SLM was used to introduce complementary phase functions into each beam and so the transverse displacement between the two images varies with defocus enabling the 3D localization of the point emitters. The truncation of the phase function and use of an SLM in [36] result in an overall transmission efficiency of 35-40%. Furthermore, the truncation of the phase function reduces the effective NA of the imaging system in one dimension and only one half of the diffraction-free range of the SB-PSF can be utilized due to a sign ambiguity.

We report a 3D particle localization technique using Airy-beam PSFs generated with a refractive cubic-phase mask (CPM) combined with image replication using a non-polarizing beam splitter to generate two replicated Airy-beam PSFs on a single detector. Unlike in [36], these PSFs are spatially extended and computational image recovery is used to generate compact images of point sources enabling a high emitter density to be imaged. The full pupil is used such that the NA and optical throughput are equal to that of an unmodified microscope (reduced only slightly by the imperfect anti-reflection coating of the two additional optical components). The implementation of the phase function using a refractive optical element offers the advantage that there is no limitation on spectral bandwidth (and so sensitivity to fluorescent emission can be maximized) and the additional component cost can be very low, in comparison to the use of an SLM. The simplicity of its implementation makes it attractive for implementation with commercial microscopes. The image recovery and depth estimation from two channels have evolved from our previously reported demonstration of extended-DOF imaging for extended scenes using the CKM technique [18, 19] (a hybrid optical-computational imaging method); thus, we refer to this technique as Airy-CKM. The extension of the depth range achieved using Airy-beam PSFs is at the cost of reduced SNR near the nominal focal plane [37] and hence on localization precision for point sources. Our emphasis here is to achieve more than an order-of-magnitude extension in depth range to enable 3D tracking of fluorescent tracer beads over extended volumes.

We demonstrate this technique using a 20×, 0.4NA microscope objective with a conventional diffraction-limited DOF of 5.8 μm, achieving an axial localization precision of better than 50 nm

Optics EXPRESS

over a depth range of 120 µm for an SNR of 46.5 dB. We believe that this constitutes the largest dynamic range reported to date, where we define dynamic range as the ratio of the axial range to axial precision. Flow measurements performed in fluorinated ethylene propylene (FEP) capillaries seeded with 0.96 µm fluorescent beads are presented where the results were found to agree well with theoretical predictions.

2. Methods

2.1. Airy-beam PSFs for 3D particle localization

The one-dimensional optical transfer function of an imaging system with a CPM in the exit pupil is [38, 39]:

$$H(u,\psi) \approx \left(\frac{\pi}{12|\alpha u|}\right)^{1/2} \exp\left(j\frac{\alpha u^3}{4}\right) \exp\left(-j\frac{\psi^2 u}{3\alpha}\right), u \neq 0, \tag{1}$$

where u is the spatial frequency, ψ is the defocus parameter and α denotes the strength parameter for the CPM (peak aberration of the cubic phase). From the Fourier-shift theorem, the linear-phase term in Eq. (1) corresponds to a defocus-dependent lateral translation equal to $\left(\frac{\psi^2 u}{3\alpha}/2\pi u\right) = \psi^2/6\pi\alpha$; therefore, in a manner analogous to the techniques employing defocus-related variations in the PSFs highlighted in the previous section, the Airy-beam PSF encodes depth information of the object as a translation of its image. The resultant translation following recovery of the image (i.e. Wiener deconvolution [40]) is:

$$T(\psi_r) = \frac{\psi_r^2 - \psi^2}{6\pi\alpha}, \tag{2}$$

where ψ_r is the defocus of the PSF used in deconvolution (the recovery kernel). Figure 1(a) depicts superimposed simulated PSFs for a two-dimensional CPM and corresponding images recovered using an in-focus PSF are shown in Fig. 1(b), where the hue indicates defocus. The translation of the recovered PSFs along the negative-unity gradient encodes the defocus and axial displacement of point (and extended) sources in the object space.

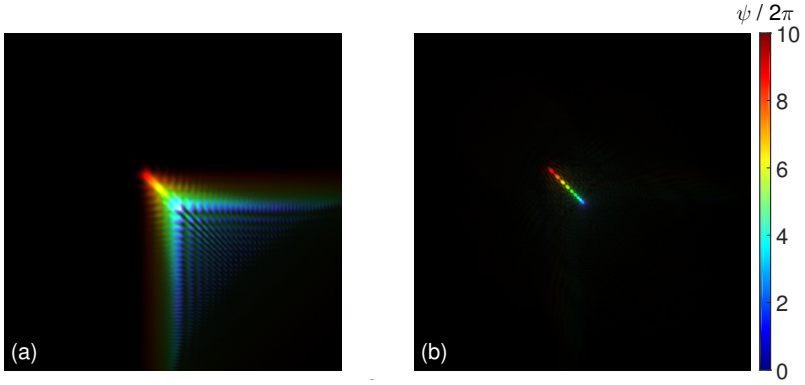

Fig. 1. (a) Simulated Airy-beam PSFs with $\alpha = 7$. (b) Corresponding recovered images (i.e., Wiener deconvolution with an in-focus PSF, $\psi_r = 0$). Colors from dark blue to dark red denote the defocus from 0 to 10 waves.

Measuring the translation requires a reference. This can be achieved by acquiring two images simultaneously on the same sensor with dissimilar image translations followed by determination of the resultant disparity. As shown in Fig. 2, a dual-focal-plane arrangement inspired by the CKM method [18] implements two distinct offsets from a nominal plane with defocus ψ to yield images with defocuses: $\psi + \Delta\psi$ and $\psi - \Delta\psi$. If we assume the image captured at $\psi + \Delta\psi$ is recovered using a kernel measured at a defocus of $\psi_r + \Delta\psi$ and correspondingly, the image

captured at $\psi - \Delta\psi$ is recovered using a kernel recorded at a defocus of $\psi_r - \Delta\psi$, then the disparity between two recovered images is

$$D(\psi_r, \psi) = T(\psi_r + \Delta\psi) - T(\psi_r - \Delta\psi) = \frac{2\Delta\psi(\psi_r - \psi)}{3\pi\alpha}, \tag{3}$$

which is proportional to $\psi_r - \psi$. Zero disparity happens if, and only if, $\psi_r = \psi$. Consequently, determining the recovery kernel which gives zero disparity yields the defocus, or equivalently, the depth of the object.

The coefficient of the image translation,

$$R = \frac{2\Delta\psi}{3\pi\alpha}, \tag{4}$$

determines the responsivity and hence sensitivity for determining defocus. Note that the responsivity is constant (i.e. it does not depend on z) over the entire depth range. Moreover, it can be adjusted by changing the defocus difference $\Delta\psi$ or the cubic phase parameter α. Note that the range for invariance of the PSF may be increased by increasing α but requires a compensating increase in $\Delta\psi$ to maintain responsivity of the disparity function.

2.2. Optical setup and data processing algorithm

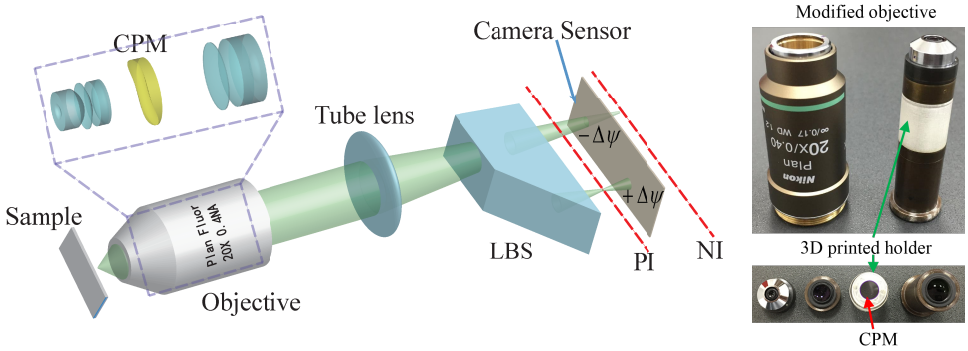

Fig. 2. (a) Schematic of the experimental setup used for three-dimensional particle localization and tracking with Airy-CKM method. CPM: cubic-phase mask; LBS: lateral beam splitter; PI: image plane of the positive imaging channel; NI: image plane of the negative imaging channel. The displacement between PI and NI for our setup was set to be 32 µm (approximately 4.9 waves). (b) Images of the modified objective, the refractive phase mask was 7×7 mm and mounted on a 3D printed holder with a circular aperture.

The proposed Airy-CKM technique was validated experimentally using an inverted microscope (*Nikon Eclipse* Ti) to characterize fluid flow in FEP capillaries. The fluid consisted of water seeded with 0.96 µm fluorescent beads excited at 480 nm and emitting at 520 nm (Bangs Laboratories, Inc. FS03F 10999). As shown in Fig. 2 , a 0.4 NA, 20× CFI Plan Achromat objective (5.8 µm DOF) was modified to accommodate a two-dimensional CPM with $\alpha = 7$ located as close as practically possible to the exit pupil (the mask was placed by trial and error at the location where measured experimental PSFs were most similar to simulated PSFs). Note that misalignment of the phase mask in xy yields aberrations such as asymmetry in the PSF [41], a 3D-printed holder was used to ensure the phase mask was well aligned to the optical axis; however, the calibration process can compensate for small misalignments and to small displacements from the exit pupil

Optics EXPRESS

position. A beam splitter was used to generate two imaging channels with a defocus offset of $+\Delta\psi$ and $-\Delta\psi$ which will be referred to hereon as the positive and the negative imaging channels respectively. The magnitude of $\Delta\psi$ was tunable by inserting a slab of glass of certain thickness into one of the optical paths. Two coded images with dissimilar focus were thus formed on the detector (*Andor Neo* 5.5 sCMOS Camera with a 2560×2160 pixel sensor), which were processed as described below to calculate the 3D location of each bead.

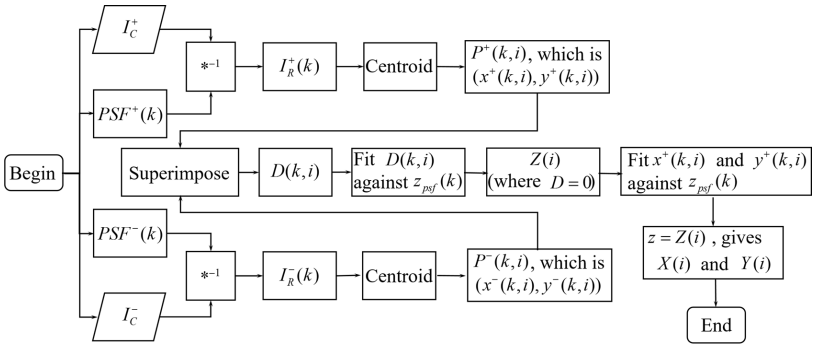

Fig. 3. Three-dimensional particle localization algorithm using Airy-CKM method. I_C^+ and I_C^- are coded images captured by the two imaging channels; $PSF^+(k)$ and $PSF^-(k)$ are the pre-recorded PSF sequences; $*^{-1}$ refers to the deconvolution operation using a Wiener filter [40]; $I_R^+(k)$ and $I_R^-(k)$ are the recovered images; $P^+(k,i)$ and $P^-(k,i)$ refer to the x-y centroids of the i^{th} particle when recovered with the k^{th} PSF; $D(k,i)$ is the disparity of the i^{th} particle in two recovered images; $X(i)$, $Y(i)$ and $Z(i)$ are the coordinates of the i^{th} particle.

The 3D-localization algorithm is illustrated in Fig. 3. Firstly, the captured coded images, I_C^+ and I_C^- were deconvolved with a sequence of calibration PSFs, $PSF^+(k)$ and $PSF^-(k)$, which were pre-acquired on their corresponding imaging channels at evenly distributed steps (3.1 μm step size) over a depth range of 150 μm. The centroids of the bead images in each channel, $P^+(k,i)$ and $P^-(k,i)$, were obtained by least-squares fit of a 2D-Gaussian function to the recovered images, I_R^+ and I_R^-. The disparity, $D(k,i)$, was calculated by taking the difference between corresponding centroids of the bead images with I_R^+ and I_R^- superimposed. A linear fit was used to determine the zero disparity point which yields the depth of the bead in the sample plane $Z(i)$.

Note that due to the defocus-related translation of the images, it is necessary to determine the actual x-y coordinates of the beads. Since the depth of each bead has been calculated, the x and y coordinates can be determined from the image translation curves in both directions which are expected to vary parabolically with depth (results shown in sec.3.2). The bead locations in 3D are thus obtained from a single snapshot.

The 3D-localization algorithm requires two-channel calibration for the measurement of disparity D, i.e. mapping between the positive and negative images, I_R^+ and I_R^-. An affine function can be used to approximate the two-channel mapping since it is dominated by a lateral shift accompanied by a magnification:

$$\begin{pmatrix} u^- \\ v^- \end{pmatrix} = A \begin{pmatrix} u^+ \\ v^+ \end{pmatrix} + \vec{c}, \tag{5}$$

where u^+ and v^+ refer to coordinates in the positive image (I_R^+) while u^- and v^- refer to the negative image (I_R^-). Point sources at the same depth yield equal image translations; thus, this calibration can be performed by recording images of many beads adhering to a single surface of a cover slip, or by imaging a single bead scanning in a single plane across the field of view (FOV)

Optics EXPRESS

using a translation stage. The calibration images are then deconvolved and the recovered points centroided to enable matrices A and $\vec{c}$ to be calculated.

3. Results and discussions

In this section, experimental results are presented, including examples of translations of the Airy-beam PSF with defocus, characterization of PSFs over an extended depth range, examples of 3D particle localization and finally particle-tracking velocimetry of fluid flow seeded with fluorescent beads within FEP capillaries.

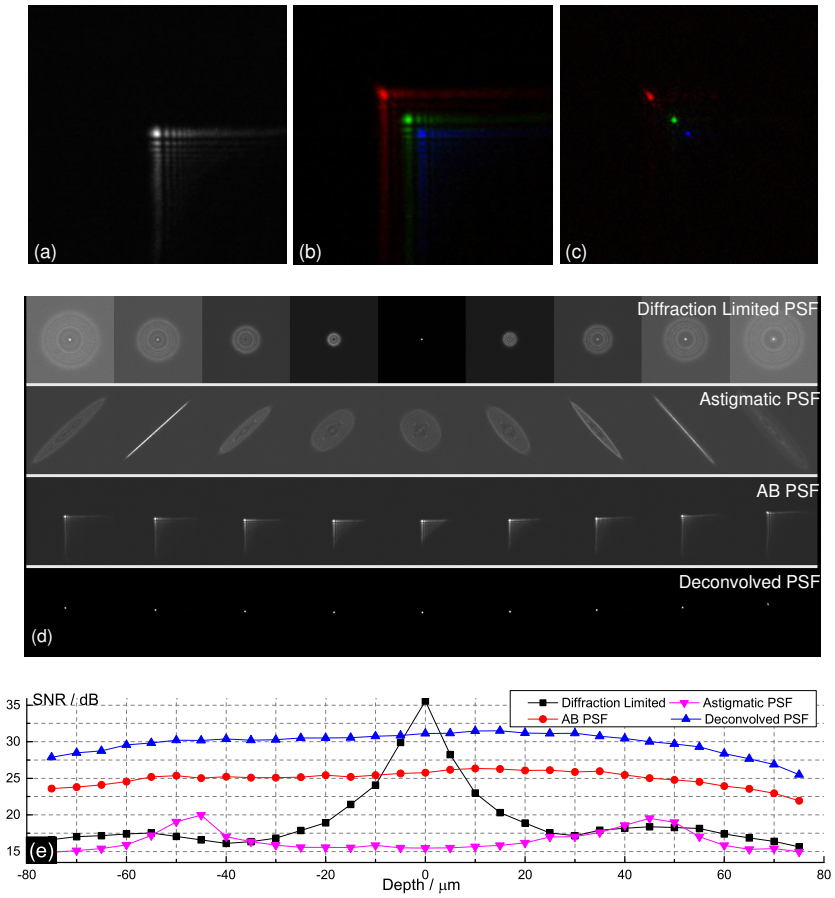

Fig. 4. (a) Image of a single in-focus bead (i.e. PSF). (b) Superimposed images of the same bead with z displacements Δz=0 (blue), 30 μm (green) and 60 μm (red) respectively. (c) Recovered images of the same bead at the mentioned depths with an in-focus PSF as the recovery kernel. (d) Comparison of the diffraction-limited PSFs, the astigmatic PSFs, the Airy-beam PSFs and the deconvolved PSFs over a depth range of 150 μm, the depth of each PSF can be read from the x axis in (e). Note that the intensity of the diffraction-limited PSFs were rescaled non-linearly to make the patterns visible. The cylindrical lens has a focal length of 1000 mm. (e) SNR comparison of the different PSFs in dB.

Optics EXPRESS

3.1. PSF translation and assessment of extended depth range

An experimental Airy-beam PSF, acquired using a single in-focus fluorescent bead, is shown in Fig. 4(a). This PSF translates along the image diagonal with varying defocus as shown in Fig 4(b) (the Cartesian axes of the CPM were aligned with the axes of the detector array). The z displacements of the bead with respect to the in-focus plane were 0 (blue), 30 µm (green), 60 µm (red) respectively. Figure 4(c) shows the images of the bead recovered from the recorded images in Fig. 4(b) using a Wiener deconvolution with the PSF in Fig. 4(a) being the recovery kernel. Since the in-focus image was deconvolved with the in-focus PSF, it yielded no translation in the recovered image (blue). However, the defocused images were deconvolved with a PSF for different defocus thus exhibiting the expected translations (green and red).

Figure 4(d) illustrates a comparison of recorded diffraction-limited PSFs, astigmatic PSFs and Airy-beam PSFs as well as deconvolved Airy-beam PSFs over a depth range of 150 µm. As can be observed, the conventional diffraction-limited PSF formed a high-peak-intensity Airy disk when it was in focus, but expanded rapidly, decreasing in intensity with increasing defocus resulting in a very limited depth range. The astigmatic PSF, which has been used in many stage-of-the-art super-resolution systems such as the *Nikon* 3D N-STORM, exhibits two focal planes yielding a continuous variation in form with changing defocus. It also expanded severely with defocus making it unsuitable for imaging of thick samples. Conversely, the intensity profile of the Airy-beam PSF changed little over the whole depth range except for the expected translation. Consequently, following deconvolution, a compact PSF was recovered for an extended depth range as shown in Fig. 4(d).

Figure 4(e) shows the variation of SNR of the recorded PSFs as a function of depth. We employ here the definition $SNR = 20\log_{10}(I_m/\sigma_b)$, where I_m is the maximum recorded intensity, and σ_b is the standard deviation of the background noise [42, 43]. The diffraction-limited PSF exhibits the highest SNR at and close to the focus; but the SNR reduced rapidly with depth, as expected, due to the rapid increase in size. Compared to the diffraction-limited PSF, the astigmatic PSF displays higher SNR at its two focal planes which were determined by the sagittal and tangential focal lengths of the imaging system. Its SNR was comparable to that of the diffraction-limited PSF when both were defocused. Conversely, the SNR of the Airy-beam PSF was approximately constant and significantly higher than that of above-mentioned techniques over the entire depth range with the exception of a 16 µm region around the focal point where the diffraction-limited PSF had a higher SNR. Furthermore, following deconvolution, the SNR was increased further and the region where the diffraction-limited PSF had a better SNR was reduced to only 7 µm. This clearly demonstrates that the Airy-beam PSF yields the highest SNR and hence most precise particle localization for operation over an extended depth range.

3.2. 3D particle localization

We discuss now the results of 3D localization of beads suspended in a microfluidic flow. Figure 5(a) shows a snapshot image of laminar fluid flow in an FEP capillary seeded with 0.96 µm fluorescent beads. FEP was used since it has a refractive index very close to that of water, effectively eradicating refraction and Fresnel reflections. The FEP capillary was oriented perpendicular to the optical axis and about 700 µm of its length was within the FOV of the microscope. The coded images, I_C^+ and I_C^-, were deconvolved using an in-focus recovery kernel (a PSF measured at $\Delta z = 0$) to obtain the recovered images I_R^+ and I_R^-, as shown superimposed in Fig. 5(b). The green and magenta dots correspond to recovered images from the positive and negative channels respectively and the red arrows indicate the calculated image disparities. As can be observed, the disparities between the recovered bead images from the two channels have a range of magnitudes indicating that the beads vary in axial displacement. The recorded and deconvolved PSFs can be seen to have forms that are independent of range as expected. The deconvolution process was repeated using a stack of calibration PSFs (i.e. $PSF^+(k)$ and $PSF^-(k)$) and a linear fit was used

Optics EXPRESS

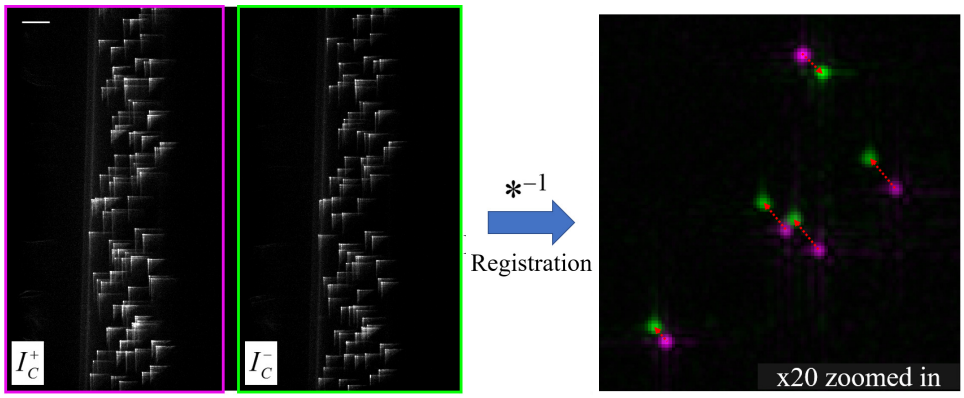

Fig. 5. (a) A snapshot of a steady laminar flow seeded with 0.96 µm fluorescent beads in an FEP capillary with a nominal inner diameter of 150 µm. The image is coded with the Airy-beam PSF and the scale bar is 50 µm. (b) Recovered images I_R^+ and I_R^- (deconvolved with the in-focus kernel) superimposed after two-channel mapping with magenta spots denoting the images recovered from positive imaging channel and green spots from the negative, 20 times zoomed in. The red arrows are the calculated image disparities.

to determine the zero crossing as previously discussed. The depth at which the recovered images yield zero disparity corresponds to the depth of the each bead.

The deconvolved image of a bead approximates the in-focus diffraction-limited point-spread function, as can be appreciated from Fig. 4(d), thus a higher seeding concentration can be obtained compared to techniques based on defocus or astigmatism (for a similar depth range). Even if the recorded PSF-coded images overlap severely as in Fig. 5(a), the recovered bead images are well isolated as in Fig. 5(b). Note that orientation of image disparities is along the unity-slope line, which can be used to unequivocally pair positive and negative images of a single particle: for example the bead images clustered in the center of Fig. 5(b) can be paired on this basis as indicated.

The z range of the system was extended to more than 150 µm by the use of the Airy-beam PSF, and any particles within this range can be precisely localized with the algorithm described in sec.2.2. Figure 6 shows a graph of the image disparity versus the depth at which the recovery kernel was recorded. The z-coordinates of the three beads (i.e. $Z1$, $Z2$ and $Z3$) were obtained from estimates of the zero-disparity point obtained by linear curve fitting. Note that the gradient of these lines (which is proportional to $\Delta\psi/\alpha$) corresponds to the responsivity of the z localization.

Once z displacement is determined, the transverse coordinates of each bead can be obtained from the image-translation curves which vary parabolically with ψ_r:

$$x - x_0 = y - y_0 \propto (\psi_r^2 - \psi^2)/6\pi\alpha, \tag{6}$$

where translations in x and y are independent. Figure 7 shows the x and y translation curves of *particle 1* (as identified in Fig. 6), for both negative and positive imaging channels. The x and y coordinates of *particle 1* can be estimated from either imaging channel $((X1, Y1)$ or $(X1', Y1'))$ in Fig. 7 since they are related by the affine function used for the two-channel mapping in Eq. (5). The coefficient of the quadratic term of the parabolas for x and y should be equal if the orientation of the principle axes of the CPM and hence the PSF is perfectly aligned with the detector array of the camera; however, an unavoidable minor angular nonalignment results in a slight difference in the shape of the x and y translation curves. Besides, the vertices of the parabolas correspond to

Optics EXPRESS

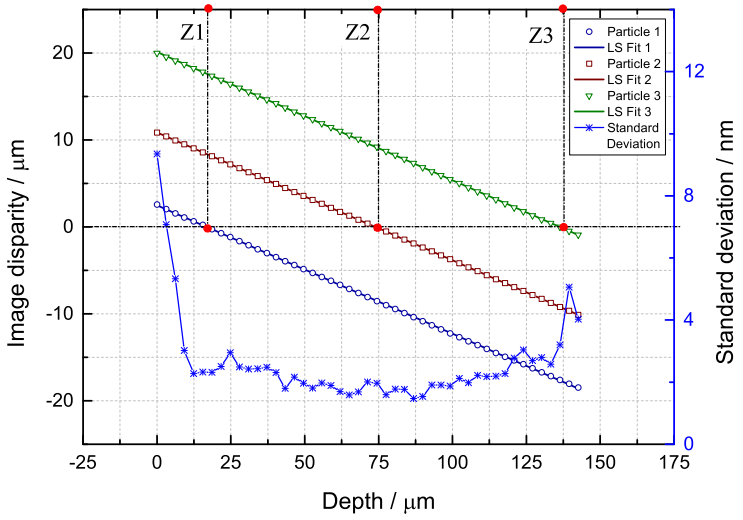

Fig. 6. Examples of the z localization process by matching the disparity of two channels. Different color corresponds to beads at different depths with scatters being the raw data, solid lines being the linear-fit results. The errors in the image disparity measurements are displayed as asterisk which were estimated within 100 frames of an immobilized bead.

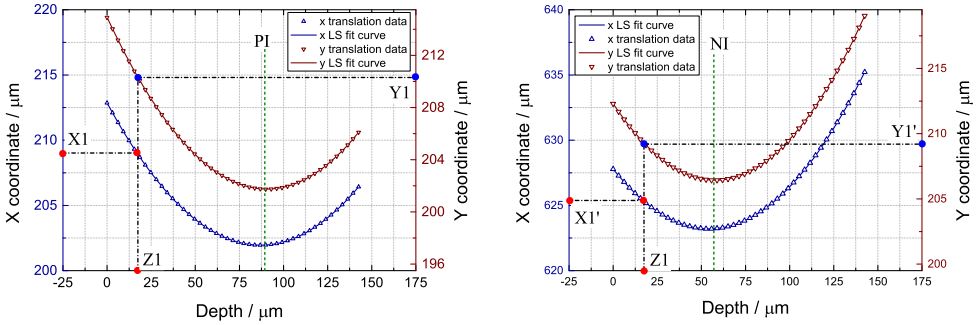

(a) positive imaging channel (b) negative imaging channel

Fig. 7. The lateral translation curves for both the imaging channels when recovered with PSFs recoded at different depths. The actual x and y coordinates can be determined from these curves once z is obtained. Blue and red curves correspond to the x and y coordinates respectively with scatters being the raw data, solid lines being the linear-fit results. PI: positive imaging plane, NI: negative imaging plane.

the image planes of the two imaging channels (PI and NI, as indicated with green lines) and their focal difference was set to be 32 μm≈4.9 waves as shown in Figs. 7(a) and 7(b).

3.3. *Localization precision analysis*

To assess the repeatability of our implementation of the Airy-CKM technique, we measured the 3D-localization precision as a function of SNR and depth. The standard deviations dropped with increasing SNR as illustrated in Fig. 8(a). For an SNR of 43.6 dB, the x, y and z precisions reached 5.1 nm×4.9nm×48.8 nm and for an SNR of 46.5 dB, an axial precision of better than 30 nm was recorded. The three histograms in Figs. 8(b)-8(d) show the distributions of the estimated x, y and z locations for 100 measurements of a single bead (Δz = 0, SNR=43.6 dB) together with

Optics EXPRESS

the Gaussian fits to the distributions. Similar to most reported experiments, the z precision is lower than the x and y precision, since the rate of change of disparity with axial position is relatively small (about 0.12, as can be seen from Fig. 6). As discussed in sec.2.1, this responsivity is tunable by changing the ratio of the focal difference $\Delta\psi$ to the cubic parameter α.

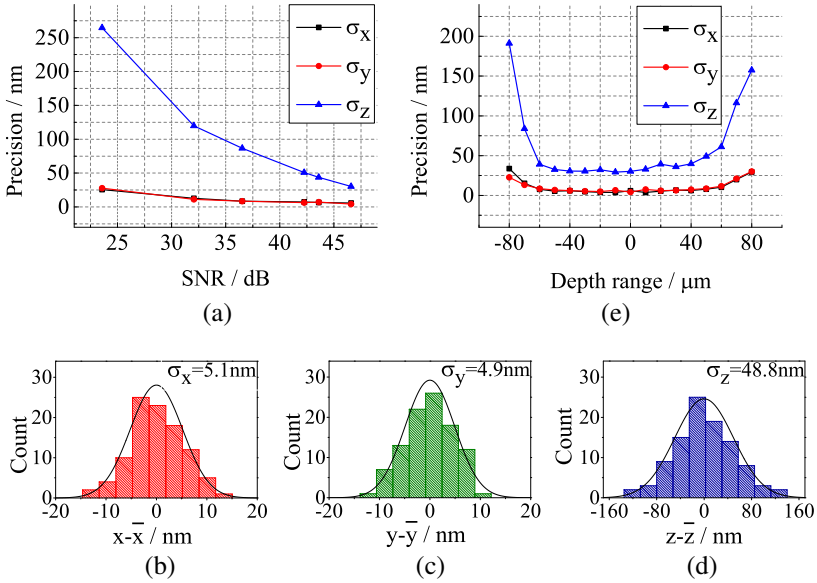

Fig. 8. Repeatability analysis from 100 measurements for each z position and each SNR. (a) Standard deviations of the x, y and z localizations of the same bead at the focal plane as a function of SNR. (b) (c) (d) Histograms of the x, y and z coordinates of the same bead at focal plane with SNR=43.6dB. (e) x, y and z standard deviations of the same bead throughout a depth range of 160 μm with an in-focus SNR of 46.5dB.

The variation of precision with z is shown in Fig. 8(e). The rapid degradation for $|z|$ >60 μm is associated with the limits of the axial range for invariance of the Airy-beam PSF and modulation-transfer function [39]. Due to the depth-insensitivity of the Airy-beam PSF for an extended range of 120 μm, an approximately constant precision of better than 50 nm is achieved in z with an in-focus SNR of 46.5 dB, and a sub-100 nm can be expected over a range of 140 μm. This is a more than 20-fold larger than the nominal DOF (5.8 μm [44]) of the objective.

The dynamic range in the axial direction is an important figure of merit for particle-tracking velocimetry: we define this as the ratio of the total measurable depth range to the precision of the measurement. Our Airy-CKM demonstration yields a dynamic range of more than 2400 in the axial direction, which we believe is the highest reported to date, exceeding the results reported with similar magnification or NA [15, 24, 45].

Note that the precision extracted is much smaller than the size of the fluorescent beads in these experiments. The SNR is emitter dependent: parameters like the emitter size and quantum yield affect the SNR and thus the localization precision. For emitters significantly bigger than the optical resolution of the system, the recovered image will become extended, reducing precision for equal number of detected photons; but the higher photon flux expected for larger emitters will tend to introduce a compensating increase in SNR and precision. The NA of the system determines the optical resolution and is a salient parameter for both the depth range and the localization precision: a lower NA yields an increased depth range, but fewer signal photons are collected resulting in a lower SNR and thus a worse precision. For applications in which single molecules are used as emitters, the number of photons collected are usually limited thus high

Optics EXPRESS

NA, high magnification and more sensitive sensor such as EMCCD are typically used.

3.4. Particle-tracking velocimetry in FEP capillaries

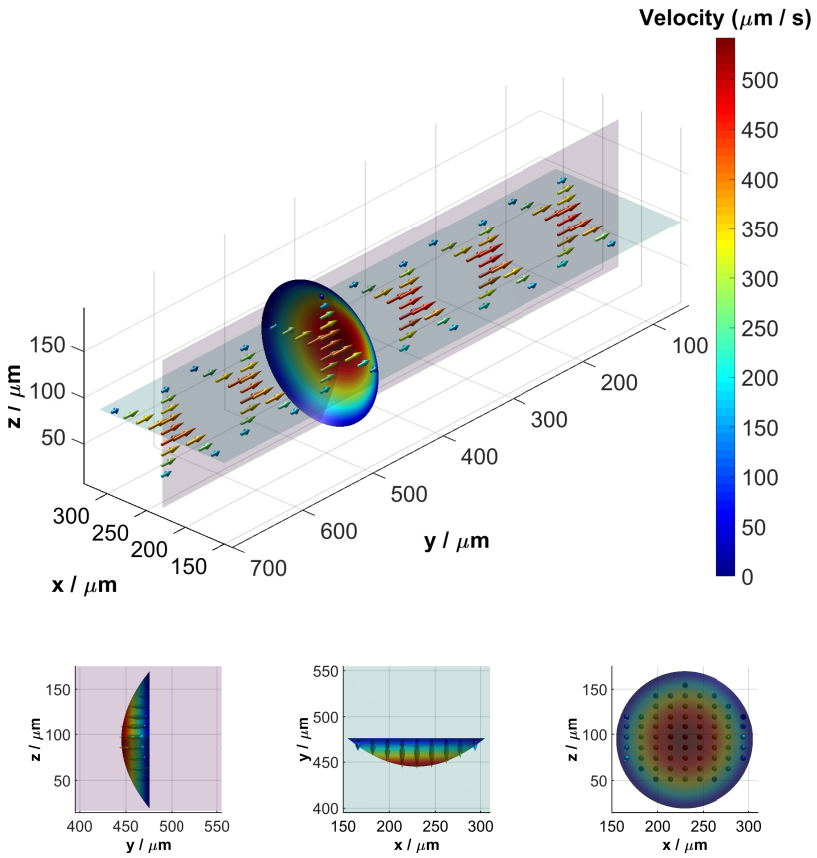

Fig. 9. 3D velocity field of a steady laminar flow generated in an FEP capillary with a nominal inner diameter of 150 µm, obtained by averaging 4000 frames at a frame rate of about 9 fps. Vectors on two perpendicular slices are shown, and the color map indicates velocities from 0 to 600 µm/s. The parabolic curve is a least-squares fit to the velocity vectors at that cross-section with its three projections shown below.

As a demonstration of the application and validity of this technique, we describe characterization of 3D fluid flow in capillaries, confirming measurements in line with predictions. Tracking particles in a flow can be performed by localizing all particles in each frame and then determining their trajectories between several successive frames. Many algorithms have been proposed for frame-to-frame particle tracking, we used a technique developed by Crocker and Grier [46], which is robust when the maximum displacement of particles between frames is less than the mean spacing between the particles.

Figure 9 shows the measured 3D velocity field for fluid flow in a 150 µm FEP capillary as described above (in Fig. 5). A syringe pump was used to generate a steady laminar flow which was seeded with 0.96 µm fluorescent beads. As required, the measured locations of all beads were within the capillary inner volume as determined from bright-field images. Since the beads

Optics EXPRESS

were relatively small and light, they did not disturb the laminar flow significantly. Consequently, the velocity profile is expected to be parabolic and is given by [47]:

$$v(r) = v_m \left(1 - r^2/R^2\right), \tag{7}$$

where v_m is the maximum velocity, r is the radial coordinate and R is the radius of the capillary. Least-squares fit of $v(r)$ yielded the profile shown in Fig. 9 together with its three orthogonal projections, which are in agreement with the expected parabolic form. The inner radius $R = 74.07\,\mu$m, obtained from curve fitting, matches the nominal inner radius of the capillary of 75 µm with an error of 1.2 %. Furthermore, we calculated $v_m = 553\,\mu\text{ms}^{-1}$ which yields a volume flow rate that is within 5 % of the value programmed into the syringe pump.

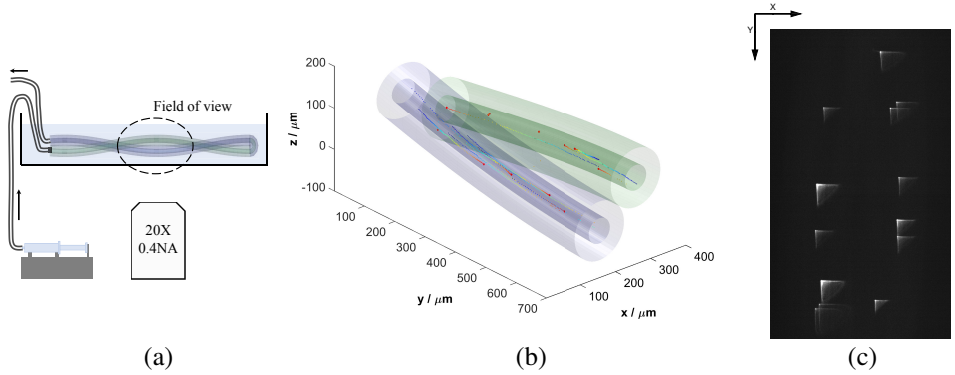

(a) (b) (c)

Fig. 10. Flow tracking in a twisted FEP capillary. (a) Twisted capillary configuration. The capillary had an inner diameter of about 50 µm and an outer diameter of about 140 µm. The capillary was immersed in salt water to match its refractive index. (b) fluorescent bead trajectories in twisted capillary within 100 successive frames. Different color denotes the time with dark blue being the first frame and dark red being the last frame. (c) image of the last frame captured by the positive imaging channel.

As a further demonstration we characterized 3D bidirectional velocity flow in two FEP capillaries that were mutually twisted to form a double helix with half a period in the 400 µm × 700 µm × 150 µm detecting volume as shown in Fig. 10(a). The capillary was stabilized on a cover-slip and immersed in saline to match the refractive index of the FEP capillary (about 1.34) and minimize refractive aberrations. Figure 10(b) shows the flow tracking of ten trajectories calculated from 100 successive frames. The hues of the trails, varying from dark blue to dark red, indicate the time evolution of their paths, clearly yielding xyz components within the helical capillaries. A relatively large red spot indicated at the end of each trajectory was from the last frame as shown in Fig. 10(c). The 3D locations were extracted from the 2D image sequences; thus, every bead in Fig. 10(b) has a corresponding PSF-coded image in Fig. 10(c). A supplemental video shows the 3D flow(see Visualization 1).

4. Conclusion

We have demonstrated a new approach for 3D particle localization and tracking based on the Airy-beam PSF generated by a single cubic-phase mask which yields the advantages of high-optical throughput and a depth range that is extended by more than 20 fold compared to the DOF of the microscope objective. In this article we have reported the localization of point sources in a 400 µm×700 µm×120 µm volume with a precision of 5 nm×5 nm×50 nm. We believe this to

Optics EXPRESS

be the highest dynamic range in the axial direction (i.e., the ratio of the detectable depth range to the axial precision) recorded to date. Since the image recovery yields a compact PSF, a high seeding concentration is more easily demonstrated than for existing techniques involving defocus and astigmatism for which the PSFs tend to be spatially extended. A particular advantage is the simplicity of this configuration which enables it to be adapted to most microscopy system.

This new technique is applicable to a wide range of applications employing particle localization, ranging from tracking of endogenous particles and fluorescent beads to localization-based super-resolution microscopy. It shows promise for flow characterization within thick biological samples, for which the required depth range normally significantly exceeds the capabilities of conventional systems. Of particular interest is the *in-vivo* characterization of cardiovascular systems, for which the zebrafish is a traditional model, due to its transparency and pertinence to human genome [48]: We will report in the near future *in-vivo* characterization of blood flow in the zebrafish. In addition, the Airy-CKM technique has potential for application to extended-range 3D localization-based super-resolution microscopy such as STORM and PALM as is described in [36], where the high optical throughput promises an improvement in the trade of depth range against localization precision. Additional advantages include extension in range due to lack of ambiguity in the sign of defocus and a simpler optical implementation employing a single refractive phase-encoding mask.

Funding

Engineering and Physical Sciences Research Council (EP/K503058/1); Leverhulme Trust (ECF-2016-757); China Scholarship Council (201503170229).